ACS OMEGA

Open Access
This article is licensed under CC-BY-NC-ND 4.0

http://pubs.acs.org/journal/acsodf
Article

Fluidized Reduction Kinetics of Boron-Bearing Iron Concentrate by Hydrogen at Low Temperatures Based on Model-Fitting and Model-Free Methods

Peiyu Li, Jianwen Yu,* Yanjun Li, Peng Gao, and Yuexin Han

Cite This: *ACS Omega* 2024, 9, 19679−19689

Read Online

ACCESS | Metrics & More | Article Recommendations

ABSTRACT: Pyrometallurgy is the most effective way to comprehensively utilize boron-bearing iron concentrate, and there is an urgency for an environmentally friendly and efficient method to achieve the prereduction of boron-bearing iron concentrate. In this study, the mechanism and kinetics of isothermal hydrogen reduction of boron-bearing iron concentrate in a fluidized bed at 500−570 °C were discussed. The reduction degree was quantified in combination with the online gas composition analysis technique, and the phase and microstructure of the reduced products were characterized. The results exhibited that the apparent activation energy remained constant during the whole reduction process, with average values of 50.67 and 48.08 kJ/mol calculated by the model-free and model-fitting methods, respectively, and the reaction was controlled by the contracting sphere model. The formation of a microporous metallic iron facilitated the rapid penetration of hydrogen to the reaction interface. Therefore, the intrinsic chemical reaction at the interface determined the whole reaction process.

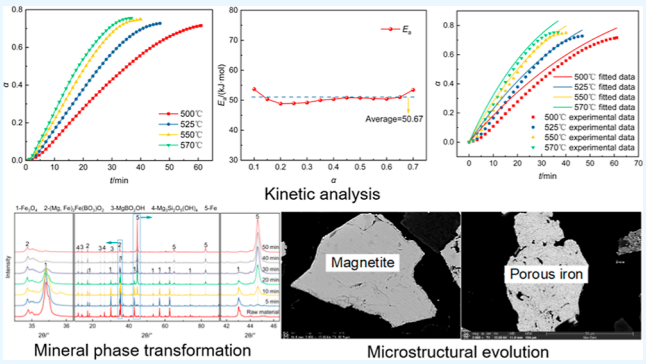

1. INTRODUCTION

Boron ore is a scarce strategic mineral resource, and boron compounds are widely used in national defense, metallurgy, nuclear energy, agriculture, construction, etc. Ludwigite ore is a multiple-element associated mineral mainly composed of iron, boron and magnesium.[1] In China, ludwigite has become a critical alternative mineral for boron materials due to the demand gap for boron compounds and the exhaustion of high-quality boron resources (e.g., szaibelyite). In Liaoning Province, the reserves of ludwigite are about 280 million tons, containing about 21.84 million tons of B_2O_3.[2] However, the beneficiation process only separates boron and iron preliminary, and the boron, which accounts for more than 30% of raw materials, enters the boron tailings, i.e., the boron-bearing iron concentrate.[3−5] Now, it is used as blending ore for blast furnaces, resulting in considerable waste of boron resources.[6]

The representative pyrometallurgical processes for the separation and utilization of boron-bearing iron concentrate include direct reduction-electric furnace smelting and reduction roasting-magnetic separation. The above methods have successfully obtained iron powder with TFe ≥90% and boron concentrate with B_2O_3 ≥14%.[7,8] Besides, the low-temperature smelting process based on supergravity obtains boron concentrates with B_2O_3 contents and recoveries exceeding 35 and 98%, respectively.[9,10] As a critical step in pyrometallurgy, coal-based reduction is typically used to reduce boron-bearing iron concentrate, which has been well-established in the iron and steel industry. The reduction kinetics of the boron-bearing iron concentrate/coal composite pellets shows that the rate-limiting step was carbon gasification at 1000−1150 °C, whereas the reduction was controlled by interfacial chemical reactions at 1150−1300 °C.[11] To achieve the metallization of boron-bearing iron concentrate, the reaction temperature exceeds 1050 °C and the reduction time is more than 1−3 h under laboratory conditions.[12−15] Therefore, the problematic aspects of reducing boron-bearing iron concentrate with coal are high reduction temperatures, energy consumption, and CO_2 emissions. With the continued global focus on carbon neutrality, the iron and steel industry strives to find alternative processes to coal-based reduction.[16] Hydrogen is considered an ideal reducing agent for iron ores, as its reduction products

Received: March 1, 2024
Revised: April 3, 2024
Accepted: April 4, 2024
Published: April 17, 2024

ACS Publications
© 2024 The Authors. Published by American Chemical Society

https://doi.org/10.1021/acsomega.4c02041
ACS Omega 2024, 9, 19679−19689

Table 1. Chemical Composition of the Sample

composition	TFe	FeO	B_2O_3	SiO_2	Al_2O_3	MgO	CaO	P	S	LOI
content (wt %)	50.94	24.31	6.44	4.70	0.25	13.31	0.51	0.011	0.833	4.63

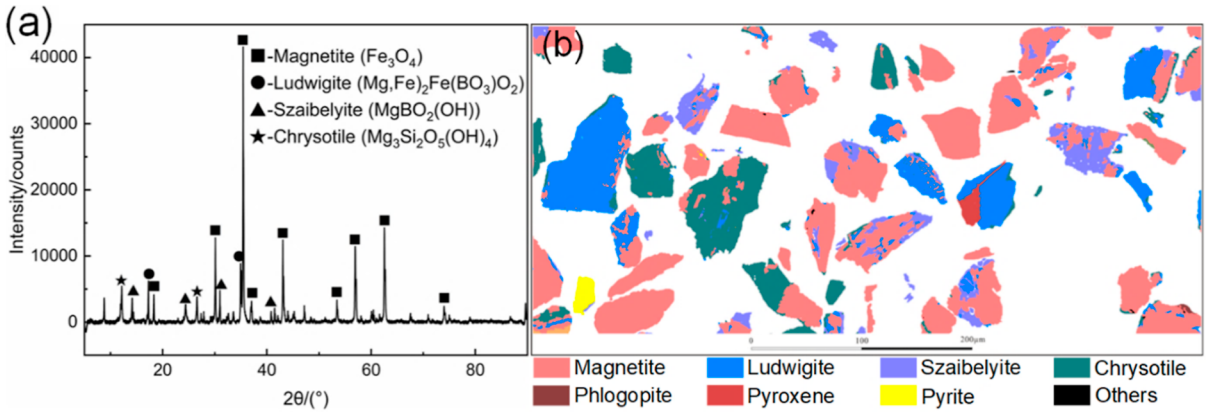

Figure 1. XRD pattern (a) and MLA image (b) of the sample.

are nonpolluting and substantially reduce carbon footprints.[17,18]

Several typical gas−solid reaction models (i.e., nucleation and growth model, phase boundary model, chemical reaction, and diffusion models) are suitable for describing the hydrogen reduction reaction of iron ores, which depends on the characteristics of raw materials such as particle size, porosity, etc., as well as the experimental apparatus.[19−22] Under normal conditions, hydrogen exhibits better reaction kinetics than carbon monoxide. As the proportion of hydrogen increases, the reaction kinetics conditions improve.[23,24] The physicochemical properties of hydrogen dictate that its diffusion rate is over three times faster than that of CO, which minimizes the adverse effects of mass transfer on the reduction.[25] However, the existing fixed bed direct reduction processes suffer from poor gas−solid mixing efficiency and slow heat and mass transfer, which reduces the kinetics advantages of hydrogen reduction.[26] In contrast, fluidized beds allow higher gas flow rates and smaller particle sizes, substantially reducing mass transfer resistance, and fluidized reduction processes such as Circored have achieved commercial applications.[27−29] Therefore, reducing iron ore with hydrogen in a fluidized bed is regarded as a promising technology for the iron and steel industry, and the reason that limits its popularization is defluidization at high temperatures.[30,31] However, the reduction of magnetite with hydrogen revealed that the dense iron layer generated at high temperatures prevented the mass transportation, whereas such retardation was absent at low temperatures, resulting in higher reduction degree.[32,33] Therefore, low-temperature metallization reduction of a boron-bearing iron concentrate with hydrogen in a fluidized bed is feasible, yet the relevant kinetic mechanism is still unclear.

In this study, combined with online gas composition analysis, the isothermal reduction kinetics with hydrogen at low temperatures (500−570 °C) was discussed, and a proper gas−solid reaction model and kinetic equations were determined by model-fitting and model-free methods. On this basis, the mineral phase and microstructure of the reduced products were characterized to confirm the validity of kinetic analysis. The results provided new insights and data support for the metallization prereduction of boron-bearing iron concentrate.

2. MATERIALS AND METHODS

2.1. Materials. The boron-bearing iron concentrate was obtained by multistep magnetic separation, and the material was screened to a particle size range of −74 to +38 μm. The chemical composition of the sample was analyzed based on chemical titration and inductively coupled plasma-mass spectrometry (Agilent 7800, Agilent Technologies Inc., American), as shown in Table 1, and the content of TFe and B_2O_3 was 50.94 and 6.44%, respectively. The main gangue components, including MgO and SiO_2, were 13.31 and 6.44%, respectively. Besides, the loss of ignition was 4.64%, indicating the presence of readily decomposable minerals in the sample.

The X-ray diffraction (XRD) pattern (PW3040, PANalytical B.V., The Netherlands) of the sample is shown in Figure 1a, and the main composition minerals were magnetite, ludwigite, szaibelyite, and chrysotile. The raw materials were set in epoxy resin and polished, and the coexistence relationship and mineral composition of the raw material were further accurately evaluated by a mineral liberation analyzer (MLA 650, FEI, American). As exhibited in Figure 1b, iron and boron minerals were closely symbiotic and magnetite was mainly associated with ludwigite, followed by szaibelyite and chrysotile. Besides, magnetite was encapsulated with irregular ludwigite and szaibelyite. According to Table 2, the iron-containing minerals were magnetite and ludwigite, with contents of 61.10 and 14.55%, respectively. The contents of szaibelyite, chrysotile, and pyrite were 11.40, 9.61, and 1.77%, respectively.

Table 2. Mineral Composition of the Sample

minerals	magnetite	ludwigite	szaibelyite	chrysotile	pyrite	others
content (wt %)	61.10	14.55	11.40	9.61	1.77	1.57

2.2. Experimental Section. *2.2.1. Experimental Procedure.* Low temperature (500−570 °C) reduction kinetics of boron-bearing iron concentrate was conducted in a fluidized reduction system, as shown in Figure 2. The reduction test was

https://doi.org/10.1021/acsomega.4c02041
ACS Omega 2024, 9, 19679−19689

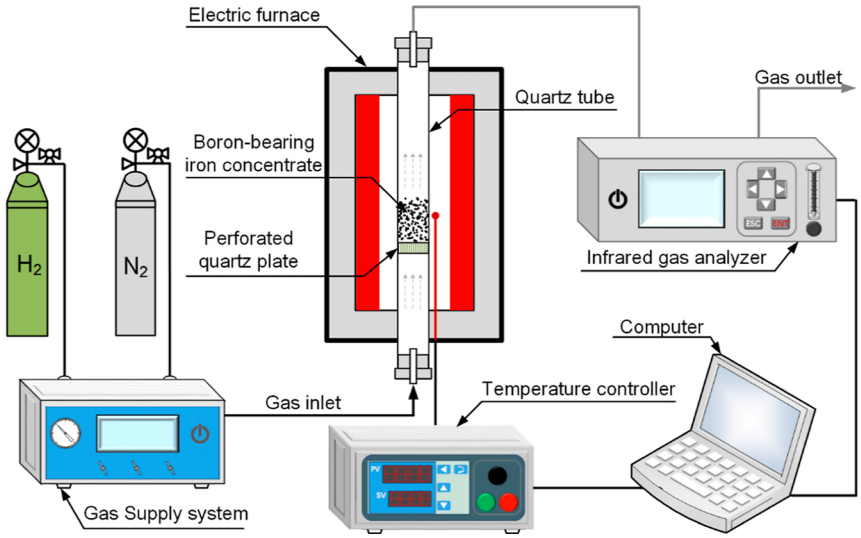

Figure 2. Schematic diagram of fluidized reduction system.

carried out under isothermal conditions. In the pre-experiment, when the H_2 concentration exceeded 80%, further increasing the H_2 concentration did not significantly promote the reaction. Therefore, the reducing gas concentration was determined to be H_2/N_2 = 80:20%, a mixture of hydrogen (99.99% purity) and nitrogen (99.99% purity), making the results closer to the intrinsic reaction kinetics. The proportion of reducing gas was precisely adjusted by a gas mass flow controller. For each experiment, 10.00 g of sample was provided into the quartz tube at a gas flow rate of 1000 mL/min to ensure fluidization. The reducing gas entered the reactor via the gas flow controller, and the exhaust gas was dehydrated and dried before entering the infrared gas analyzer. When the infrared gas analyzer showed that the H_2 concentration was stabilized at 80%, the quartz tube was immediately placed into the furnace that reached the preset temperature to conduct the fluidized reduction test, and the residual H_2 content of the exhausted gas was monitored in real-time. The first 1 s before the H_2 concentration in the exhaust gas started to decrease was considered the zero moment of the reaction with a data recording interval of 1 s. At the end of each experiment, the sample was cooled under a nitrogen atmosphere and transferred to a sealed bag.

2.2.2. Data Analysis. The weight loss of the samples was challenging to measure under fluidized conditions. Hence, the quantitative changes in the reduction process were continuously verified using infrared gas analysis (Gasboard-3100, Cubic-Ruiyi, China) for the kinetic data evaluation. The advantage of gas composition analysis over chemical titration analysis was the continuous collection of reduction data from a single sample, which undoubtedly reduced the number of kinetic calculation errors.

During the reduction process, the decrease of H_2 concentration in exhausted gas was due to the formation of water by transferring O atoms from the raw material to H_2, as shown in eq 1:[34]

$$Fe_3O_4(s) + 4H_2(g) = 3Fe(s) + 4H_2O(g)(T \leq 843\ K) \tag{1}$$

Based on the change in H_2 concentration, the instantaneous consumption of reaction gas is obtained by conversion. The instantaneous hydrogen flow rate is shown in eq 2

$$x_t = \left(\frac{200 \cdot C_t}{100 - C_t}\right)/60 \tag{2}$$

where x_t is the H_2 flow rate at time t, mL/s, C_t is the H_2 concentration at time t,%, and 200 is a constant N_2 flow rate, mL/min.

The initial hydrogen flow rate is 13.33 mL/s, and the instantaneous hydrogen consumption Q_t is shown in eq 3

$$Q_t = 13.33 - x_t \tag{3}$$

The calculation method of reaction conversion degree (α) is shown in eq 4

$$\alpha = \frac{V_t}{V_{theory}} = \frac{\sum_{i=0}^{t} Q_i \Delta t}{V_{theory}} \tag{4}$$

where α is the conversion degree at t min, V_t is the cumulative gas consumption at t min (mL), i is the i min of the reduction reaction ($0 \leq i \leq t$, min), Q_i is the instantaneous consumption of H_2 at i min, Δt is the data record interval (1 s, 1/60 min). Besides, V_{theory} represents the theoretical H_2 consumption for completely reducing the sample to metallic iron. The dosage for each experiment is 10.0 g, and the Fe^{2+} and Fe^{3+} contents in the sample are 17.45 and 33.49%, respectively. Therefore, the V_{theory} value is 2678.11 mL.

2.2.3. Kinetic Analysis. The reduction rate (r) of gas−solid reactions can be described by the differential of conversion degree (α) and time (t)

$$r = \frac{d\alpha}{dt} = k(T)f(\alpha) \tag{5}$$

where $k(T)$ is the reaction rate constant at temperature T, and $f(\alpha)$ is the differential form of the mechanism model.

According to Arrhenius formula, the relationship between $k(T)$ and T is described as

$$k(T) = A\exp\left(-\frac{E_a}{R \cdot T}\right) \tag{6}$$

where A, E_a and R represent pre-exponential factor (min^{-1}), apparent activation energy (J/mol) and universal gas constant (8.314 $J/mol^{-1} \cdot K^{-1}$), respectively.[35,36]

Substituting eq 6 into eq 5, and $d\alpha/dt$ is given in eq 7

https://doi.org/10.1021/acsomega.4c02041
ACS Omega 2024, 9, 19679−19689

Table 3. Gas−Solid Reaction Kinetic Models Derived from Different Rate-Limiting Mechanisms

model	symbol	description	formula of $f(\alpha)$	formula of $G(\alpha)$
nucleation and nuclei growth	A1	Avrami-Erofeev (m = 1) model	$1-\alpha$	$-\ln(1-\alpha)$
	A2	Avrami-Erofeev (m = 2) model	$2(1-\alpha)[-\ln(1-\alpha)]^{1/2}$	$[-\ln(1-\alpha)]^{1/2}$
	A3	Avrami-Erofeev (m = 3) model	$3(1-\alpha)[-\ln(1-\alpha)]^{2/3}$	$[-\ln(1-\alpha)]^{1/3}$
phase boundary	R1	contracting disk	1	$1-(1-\alpha)^{1/1}=\alpha$
	R2	contracting cylinder	$2(1-\alpha)^{1/2}$	$1-(1-\alpha)^{1/2}$
	R3	contracting sphere	$3(1-\alpha)^{2/3}$	$1-(1-\alpha)^{1/3}$
chemical reaction order-based	F2	second order	$(1-\alpha)^2$	$(1-\alpha)^{-1}-1$
	F3	third order	$1/2(1-\alpha)^3$	$(1-\alpha)^{-2}-1$
diffusion	D1	one-dimensional diffusion model	$1/2\alpha^{-1}$	α^2
	D2	two-dimensional diffusion model	$[-\ln(1-\alpha)]^{-1}$	$\alpha+(1-\alpha)\ln(1-\alpha)$
	D3	three-dimensional diffusion model (Jander eq.)	$3/2(1-\alpha)^{2/3}[1-(1-\alpha)^{1/3}]^{-1}$	$[1-(1-\alpha)^{1/3}]^2$
	D4	three-dimensional diffusion model (Ginstein-Brounshtein eq.)	$3/2[(1-\alpha)]^{-1/3}-1]^{-1}$	$1-2/3\alpha-(1-\alpha)^{2/3}$

$$\frac{d\alpha}{dt}=A\exp\left(-\frac{E_a}{R\cdot T}\right)f(\alpha) \tag{7}$$

Integrating both sides of eq 5, the integral form $G(\alpha)$ of the mechanism function is shown in eq 8

$$G(\alpha)=\int_0^{\alpha}\frac{d(\alpha)}{f(\alpha)}=A\exp\left(-\frac{E_a}{R\cdot T}\right)t=k(T)t \tag{8}$$

The appropriate model is determined based on the linear correlation coefficient of the $G(\alpha)$ value and time t (the function model of gas−solid reaction is shown in Table 3).[37] The fitted line with the highest R^2 indicates the probable mechanism model, and the slope of the line is $k(T)$ at the corresponding temperature. Taking the logarithms on both sides of eq 6 yields eq 9

$$\ln k(T)=\ln A-\frac{E_a}{R}\cdot\frac{1}{T} \tag{9}$$

Equation 9 reveals that $\ln k(T)$ and $1/T$ are linearly related. After linear fitting of $\ln k(T)$ and $1/T$ for each temperature, the slope of the fitted line is $-E_a/R$, and the intercept is $\ln A$. Therefore, the apparent activation energy E_a and pre-exponential factor A values of the reaction model are determined.

As briefly stated above, fitting experimental data to existing models to determine the values of $G(\alpha)$, E_a and A is the most commonly used method for treating isothermal kinetic parameters. Despite the model-fitting method allowing for the rapid determination of the whole kinetic parameters among existing models, the limitation is that the kinetic triplets obtained in such a way are the average value of the whole reaction process, which cannot reflect the variation of the kinetic mechanism with the reaction degree.

As a kinetic supplementary method, the iso-conversion (model-free) method allows the reaction process to be determined as a function between activation energy and conversion degree without considering the kinetic model.[38] The relationship between activation energy and conversion degree can be obtained by linearly fitting the time and temperature when a specific conversion rate is reached.[39,40] The most common model-free method is acquired by taking the natural logarithm of both sides of eq 8

$$\ln t_\alpha=\frac{E_a}{RT}+\ln\frac{G(\alpha)}{A} \tag{10}$$

Therefore, considering $G(\alpha)$ and A as constants, the value of E_a at the corresponding α can be calculated. In this work, the model-free method was used to determine the value of E_a initially, and variation of E_a revealed that the reaction proceeded in several steps. Then, the model-fitting method was applied to determine the mechanism model, and the reaction rate-limiting step was inferred through the selected model. Besides, the values of E_a derived from the model-free and the model-fitting methods should be approximately equal at the same reduction stage.

3. RESULTS AND DISCUSSION

3.1. Conversion Degree. The relationship between conversion degree and time during isothermal reduction of the boron-bearing iron concentrate at different reduction temperatures is shown in Figure 3. The elevation of temperature promoted the reduction kinetics, and the time required to reach the same conversion degree was drastically shortened. When the reduction temperature was 500 °C and the α value was 0.70, the reduction time was 56.83 min, while at 570 °C it was drastically reduced to 28.78 min. As a comparison, the reduction degree of boron-bearing iron concentrate reduced by coal at 1000 °C for 30 min was about 0.5, and hydrogen reduction significantly reduced the reaction temperature.[11] However, the increase in conversion degree was difficult when the α exceeded 0.72, suggesting that

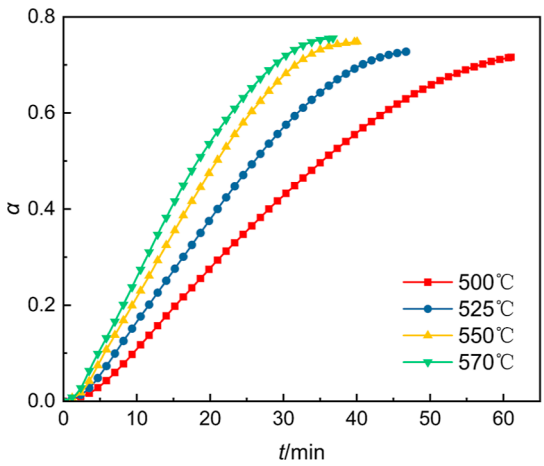

Figure 3. "α vs t" graphs of boron-bearing iron concentrates for various temperatures.

https://doi.org/10.1021/acsomega.4c02041
ACS Omega 2024, 9, 19679−19689

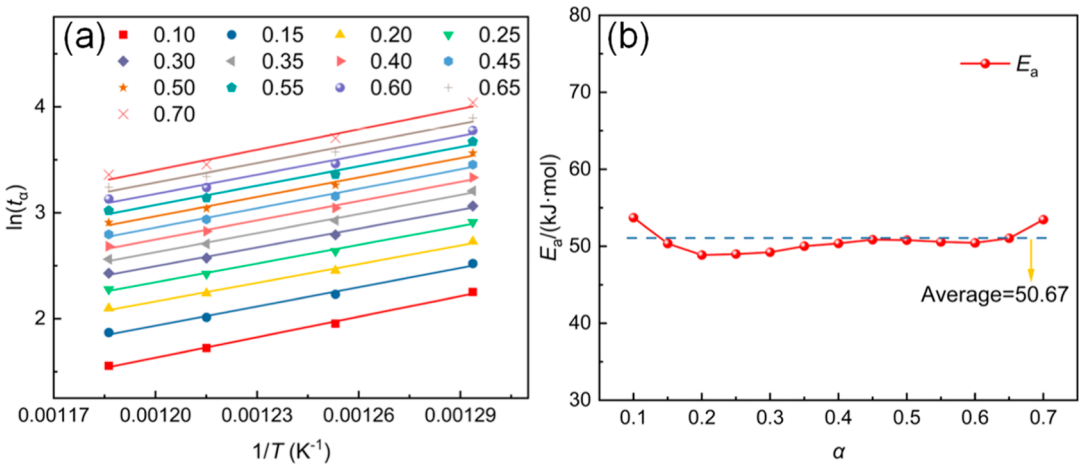

Figure 4. "ln(dα/dt) vs 1/T" graph for isothermal reduction (a) and reaction activation energy (b).

the boron-bearing iron concentrate could not be reduced entirely in this temperature range.

3.2. Evaluation of Apparent Activation Energy. The ln(t_α) and 1/T curves at various temperatures are given in Figure 4a, and the apparent activation energy calculated from the slope of the fitted line is presented in Figure 4b.

The linear correlation between ln(dα/dt) and 1/T for different temperatures was promising, and the R^2 of the fitted lines was superior to 0.99. The average value of E_a calculated by the model-free method was 50.67 kJ/mol, which was much lower than that of coal-based reduction of boron-bearing iron concentrate (70.13−164.26 kJ/mol), demonstrating superior kinetic conditions for hydrogen reduction.[11,41] Notably, the E_a value showed a slight variation throughout the reduction, which implied that there was no significant transformation of the reaction mechanism or rate-limiting step throughout the reaction.

3.3. Determination of the Kinetic Model. The activation energy of the reaction did not change significantly during the entire reduction stage. Therefore, the overall reaction kinetic data were taken into the multiple models shown in Table 2, and then the $G(\alpha)$ values were calculated and plotted against t. The appropriate mechanism model (with the highest R^2) was derived by examining the degree of fitting of the experimental data to the various models, and the corresponding results are given in Figure 5.

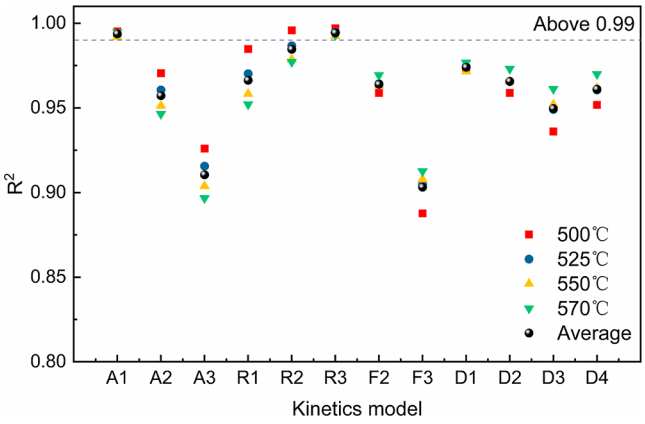

Figure 5. Linear correlation coefficients (R^2) were obtained by fitting various models.

The R^2 of the A1 and R3 models was superior to 0.99 at each temperature, with average values of 0.9938 and 0.9943, respectively, suggesting that the mechanism function of the reduction reaction may be one of the above. Figure 6a,b shows the fitting results of the A1 and R3 models, respectively, which exhibit a well-fitted linear relationship with time. If the reaction was controlled by a certain mechanism model, then the relationship between $G(\alpha)$ and t should be approximately straight. Based on the slope of straight lines in Figure 6, the corresponding reaction rate constants $k(T)$ were calculated, as given in Table 4.

In either model, the $k(T)$ was positively correlated with the reduction temperature, which indicated that increasing the temperature favored the reduction reaction. According to eq 7, plotted against ln$k$ and 1/T, the activation energy and pre-exponential factor of the corresponding model were calculated, and the results are summarized in Figure 7.

The apparent activation energies calculated by the A1 model and R3 model were 47.37 and 48.08 kJ/mol, respectively, which were close to the model-free method results (50.67 kJ/mol). Therefore, the above results were insufficient to conclude which mechanism model was most consistent with the experimental data. To solve this, $G(\alpha)$ of different reaction models was brought into eq 8, and α was solved inversely, as shown in eqs 11 and 12

$$\mathrm{A1}\alpha = 1 - \exp\left(-A\exp\left(\frac{-E_a}{R\cdot T}\right)t\right) \tag{11}$$

$$\mathrm{R3}\alpha = 1 - \left(1 - A\exp\left(\frac{-E_a}{R\cdot T}\right)t\right)^3 \tag{12}$$

Besides, a root-mean-square deviation (RMSD) was introduced as a quantitative measure of the accuracy of the fitted values, as shown in eq 13

$$\mathrm{RMSD} = \sqrt{\frac{\sum_{i=1}^{n}(y_{\mathrm{exp}.i} - y_{\mathrm{cal}.i})^2}{n}} \tag{13}$$

where $y_{\mathrm{exp}.i}$ is the experimental value; $y_{\mathrm{cal}.i}$ is the model calculation value; n is the number of data points.[37]

The comparative results of the model fitted, experimental values, and RMSD analysis are shown in Figure 8 and Table 5, respectively. Figure 8 indicates that the coincidence degree of the R3 model was higher than that of A1. Furthermore, smaller

https://doi.org/10.1021/acsomega.4c02041
ACS Omega 2024, 9, 19679−19689

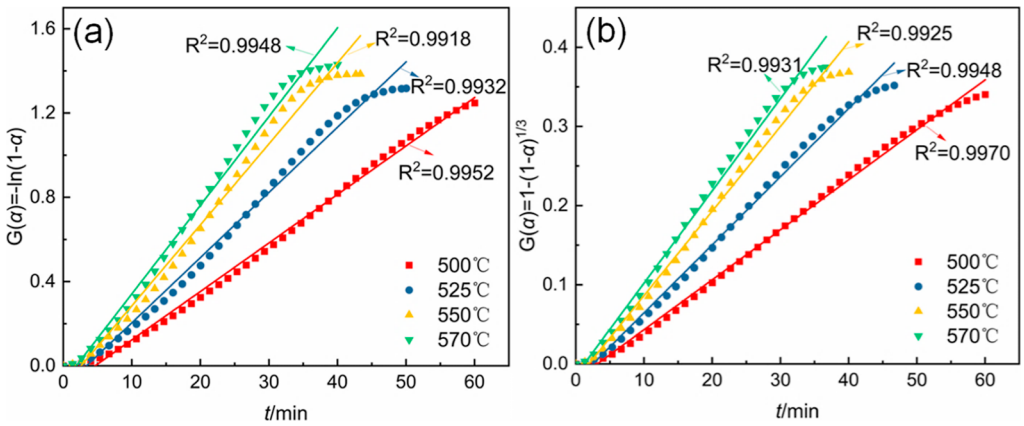

Figure 6. Dependence of possible mechanism model on reaction time: (a) A1 model; (b) R3 model.

Table 4. k and R^2 Corresponding to Different Mechanism Functions

mechanism function	K (°C)	$k(T)$ (min^{-1})	R^2
A1: $G(\alpha) = -\ln(1-\alpha)$	773 (500)	0.02301	0.9952
	798 (525)	0.03094	0.9932
	823 (550)	0.03845	0.9918
	843 (570)	0.04211	0.9948
R3: $G(\alpha) = 1-(1-\alpha)^{1/3}$	773 (500)	0.00631	0.9970
	798 (525)	0.00860	0.9948
	823 (550)	0.01068	0.9925
	843 (570)	0.01166	0.9931

RMSD values represented a better fit, as the model predictions were approximated to the experimental data. Therefore, the shrinking unreacted core mode R3 was determined as the most probable reduction mechanism. The shrinking core model assumed that the boron-bearing iron concentrate particles were initially surrounded by hydrogen and that the reaction occurred only at the surface. As the reaction proceeded, the core of the particle was surrounded by a continuous generation of metallic iron product, suggesting a gradual progression of the reaction interface toward the magnetite core, and that the reaction was controlled by the reaction rate at the magnetite and metallic iron reaction interface.

By substituting the above-determined $f(\alpha)$, values of E_a and A into eq 7, the fluidized reduction kinetics of boron-bearing iron concentrate at 500−570 °C was acquired, as shown in eq 14

$$\frac{d\alpha}{dt} = 34.77\exp\left(-\frac{48.08}{RT}\right)(1-\alpha)^{2/3} \tag{14}$$

3.4. Reduction Mechanism. To further validate the kinetics and elucidate the reaction mechanism, the boron-bearing iron concentrate was reduced at 550 °C for various times (5, 10, 20, 30, 40, and 50 min), and the mineral phase composition, micromorphology, and pore characteristics of the reduced products were investigated by XRD, scanning electron microscopy-energy-dispersive system (SEM-EDS) (Apreo 2C, Thermo Scientific, American) and a specific surface area analyzer (Asap 2460, Micromeritics, American), respectively.

3.4.1. Mineral Phase Transformation. Figure 9 displays the XRD patterns of the samples at various times. After 5 min of reduction, the diffraction peaks of magnetite weakened slightly, the diffraction peak of (110) crystal plane of metallic iron appeared at $2\theta = 44.67°$, and no wüstite was present during the reduction of magnetite to metallic iron. The diffraction peaks of the (200) and (211) crystal planes of metallic iron at $2\theta = 65.02$ and 82.34°, respectively, were observed with increasing reduction time, and the diffraction intensity increased sharply. Conversely, the diffraction peaks of magnetite weakened continuously and were approximately unidentified at 40 min, indicating that the reduction of magnetite was achieved. Further extended to 50 min, the diffraction peak in the XRD spectrum was consistent with that observed for 40 min.

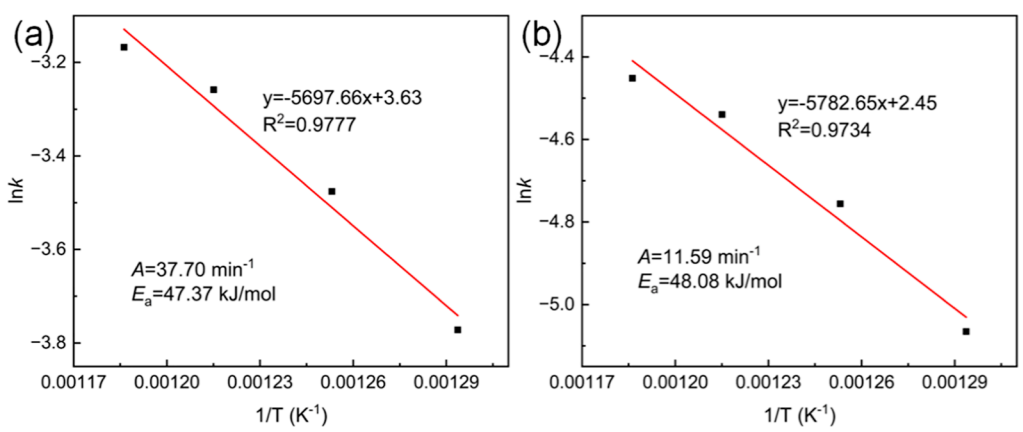

Figure 7. Linear fitting of ln$k$ vs $1/T$: (a) A1 model; (b) R3 model.

https://doi.org/10.1021/acsomega.4c02041
ACS Omega 2024, 9, 19679−19689

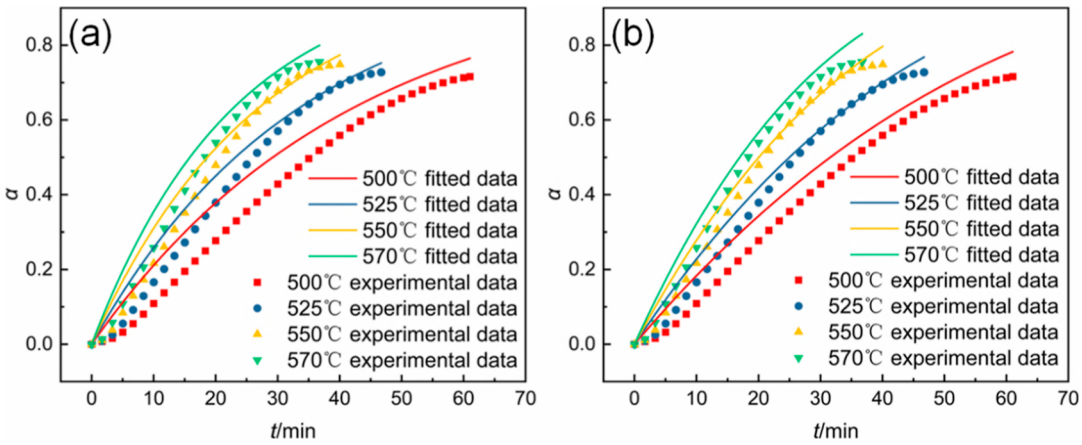

Figure 8. Comparison between the model fitted value and experimental value: (a) A1 model; (b) R3 model.

Table 5. RMSD Analysis of the A1 Model and R3 Model

mechanism function	RMSD				
	temperature/K (°C)				
	773 (500)	798 (525)	823 (550)	843 (570)	average
A1	0.07438	0.05821	0.05599	0.06021	0.06220
R3	0.05427	0.03846	0.03804	0.04604	0.04420

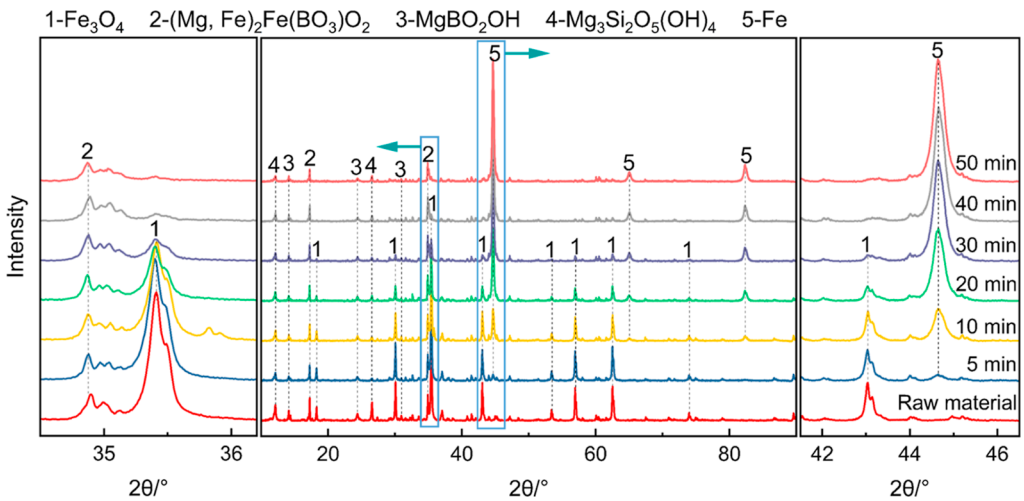

Figure 9. XRD patterns of boron-bearing iron concentrate reduced at 550 °C and various times.

Significantly, the intensity of ludwigite peaks [(120) and (240) crystal planes] was essentially nonaltering throughout the reduction process, suggesting that the high-valent iron in the ludwigite phase was not reduced to 0-valent iron by hydrogen at this temperature. It explains the difficulty in increasing the reduction degree after reaching 0.72 in the reaction kinetics; i.e., the magnetite in the boron-bearing iron concentrate was reduced, while the ludwigite, which accounted for 14.55% of the raw material, was not reduced at all. Moreover, the literature reported that the complete dehydration temperature of szaibelyite and chrysotile was above 600 °C.[42,43] Therefore, a slight decrease in the intensity of szaibelyite and chrysotile diffraction peaks was observed due to an insufficient decomposition temperature.

3.4.2. Microstructural Characterization. Figures 10 and 11 show the SEM images and the corresponding EDS results of the samples reduced at 550 °C at various times. According to Figure 10a,b, the dense structure of magnetite particles was destroyed from the outermost layer at 5 min, and a microporous structure was developed at the edge of the particle. The EDS results confirmed that the region with a pore structure was metallic iron, indicating that hydrogen reduced the outermost magnetite layer. At 10 min (Figure 10d,e), the area of the particles reduced to metallic iron increased significantly, and the cracks that were originally present in the particles also acted as mass transfer channels to facilitate the reduction. As shown in Figure 10g,h, at 20 min, the magnetite was encapsulated by porous products and hydrogen diffused through the porous iron toward the reaction interface, which resulted in the gradual shrinkage of the unreacted core. Besides, the ludwigite was structurally intact and dense, which supported the XRD results that the ludwigite could not be reduced by hydrogen in this temperature range.

As the reduction proceeded, the unreacted magnetite core shrunk into a narrow area (Figure 11a,b), and the portion that was reduced to metallic iron was covered with micropores. At

https://doi.org/10.1021/acsomega.4c02041
ACS Omega 2024, 9, 19679−19689

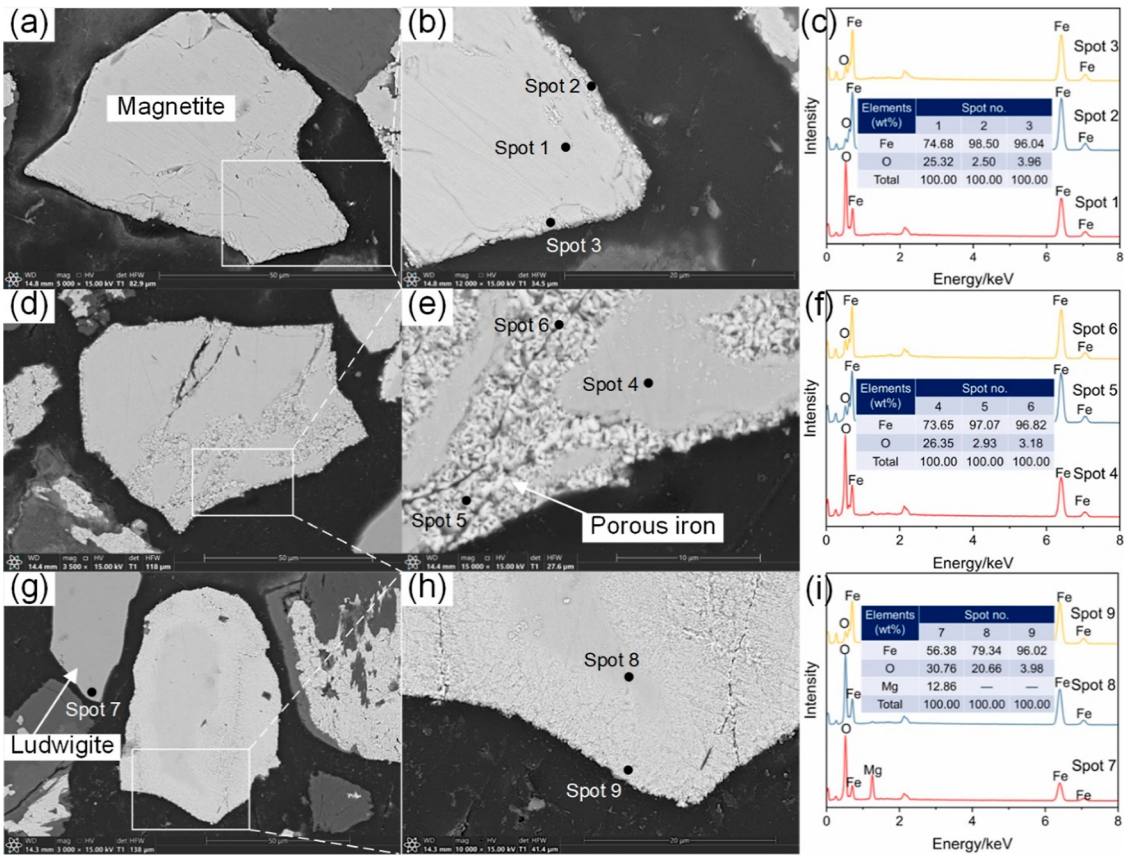

Elements (wt%)	Spot no. 1	2	3
Fe	74.68	98.50	96.04
O	25.32	2.50	3.96
Total	100.00	100.00	100.00

Elements (wt%)	Spot no. 4	5	6
Fe	73.65	97.07	96.82
O	26.35	2.93	3.18
Total	100.00	100.00	100.00

Elements (wt%)	Spot no. 7	8	9
Fe	56.38	79.34	96.02
O	30.76	20.66	3.98
Mg	12.86	—	—
Total	100.00	100.00	100.00

Figure 10. SEM-EDS results of boron-bearing iron concentrate reduced at 550 °C and various times: (a−c) 5; (d−f) 10; (g−i) 20 min.

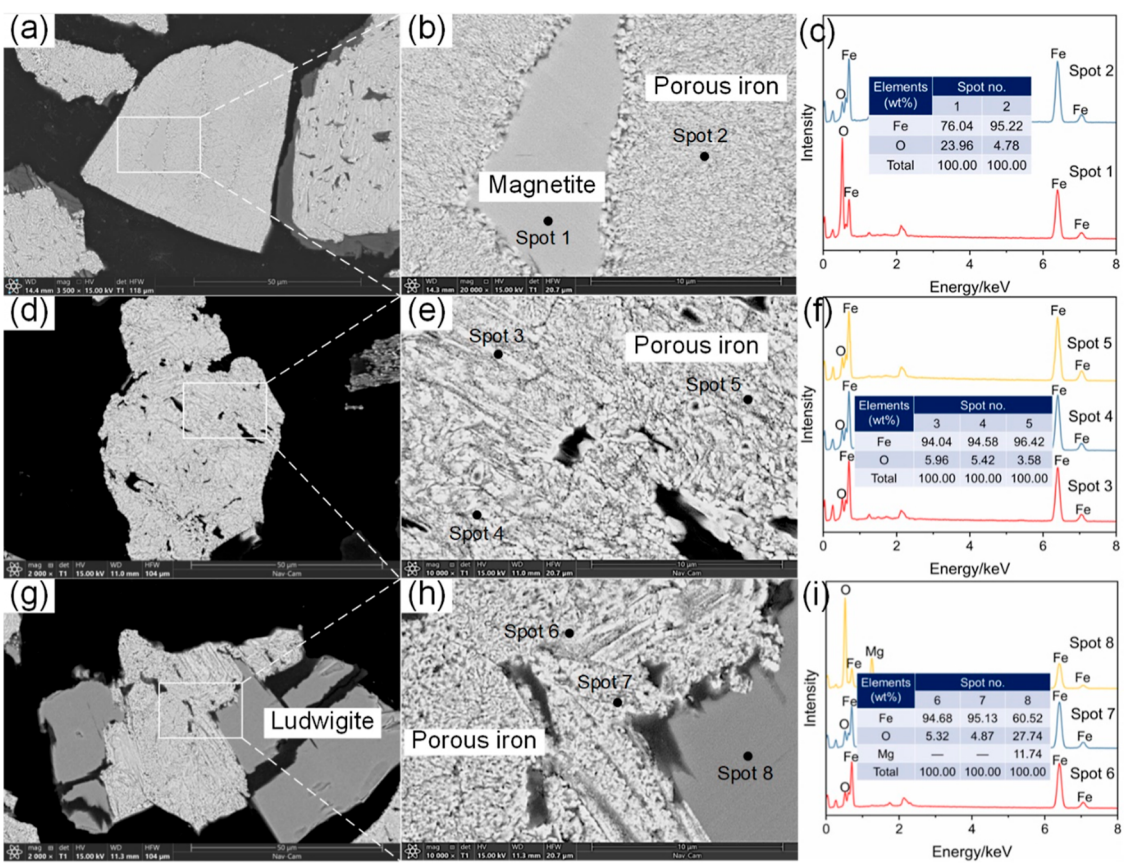

Elements (wt%)	Spot no. 1	2
Fe	76.04	95.22
O	23.96	4.78
Total	100.00	100.00

Elements (wt%)	Spot no. 3	4	5
Fe	94.04	94.58	96.42
O	5.96	5.42	3.58
Total	100.00	100.00	100.00

Elements (wt%)	Spot no. 6	7	8
Fe	94.68	95.13	60.52
O	5.32	4.87	27.74
Mg	—	—	11.74
Total	100.00	100.00	100.00

Figure 11. SEM-EDS results of boron-bearing iron concentrate reduced at 550 °C and various times: (a−c) 30; (d−f) 40; (g−i) 50 min.

https://doi.org/10.1021/acsomega.4c02041
ACS Omega 2024, 9, 19679−19689

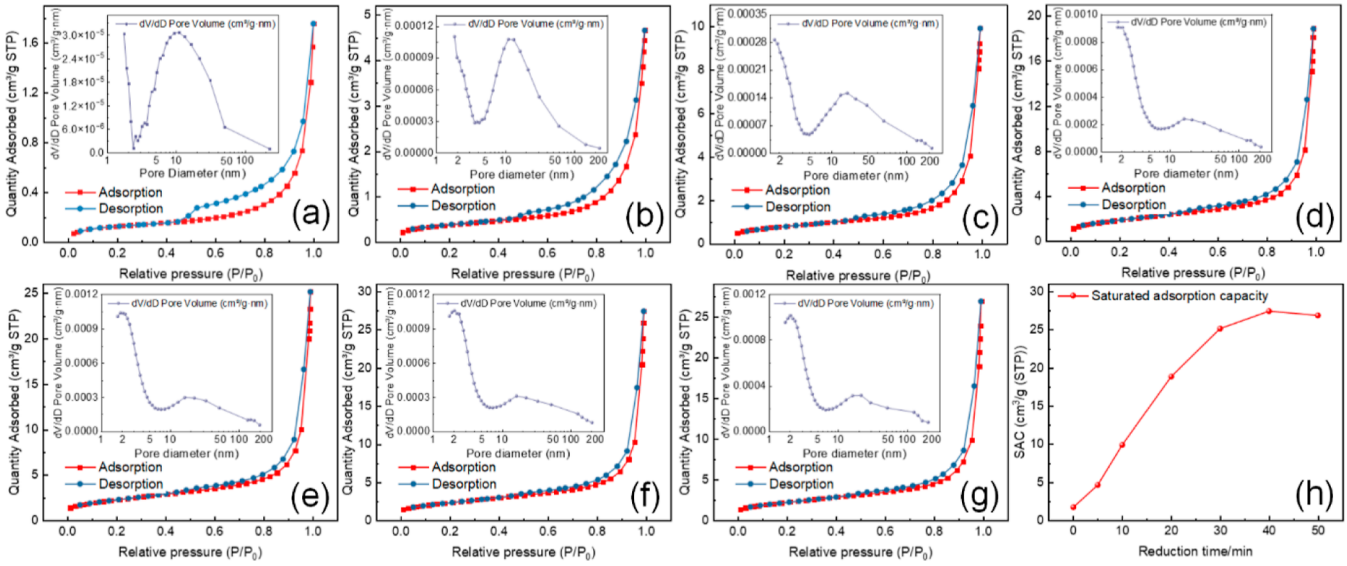

Figure 12. N_2 adsorption and desorption isotherms and mesopore size distribution of boron-bearing iron concentrate with different reduction times at 550 °C: (a) raw material; (b) 5; (c) 10; (d) 20; (e) 30; (f) 40; (g) 50 min; (h) SAC.

40 min, the magnetite at the inner core was entirely reduced by hydrogen, as the porous iron acted as the mass transfer channel. After further prolonging to 50 min, the structure of metallic iron was almost unchanged, while the ludwigite remained unreacted. Therefore, in the whole reduction process of the boron-bearing iron concentrate, the rate-limiting step was the reaction progress at the magnetite-metallic iron phase interface since the ludwigite did not participate in the reaction. The reduction of the particles was consistent with the contracting sphere model, which verified the correctness of the kinetic analysis.

3.4.3. Pore Characteristics. The pore parameters of the samples were analyzed using the Brunauer–Emmett–Teller and Barrett–Joyner–Halenda (BET–BJH) method.[44] Figure 12 shows the N_2 adsorption–desorption isotherms and BJH pore size distributions of the samples at 77 K. According to the IUPAC classification, the isotherms of the samples were all of the IV category with type 3 hysteresis loops, which may feature a distribution of slit-shaped pores.[45] The saturated adsorption capacity (SAC) of the samples increased nearly linearly with the reduction time and reached the maximum in 40 min, indicating a significant increase in porosity. The pore size distribution reflected that mesopores of 10–30 nm dominated the pores of the samples. Besides, as the reduction proceeded, the pore distribution presented a prominent band near 2–3 nm, implying substantial micropore formation.

The pore parameters of the samples are shown in Table 6. The raw material was structurally dense with a BET surface area and total pore volume of only 0.4754 m^2/g and 0.0024 cm^3/g, respectively. When the raw material was contacted with hydrogen and reacted for 5 min, porous metallic iron was rapidly formed and the BET surface area and total pore volume increased significantly to 1.3683 m^2/g and 0.0072 cm^3/g, respectively. With the continuous formation of porous metallic iron, the BET surface area and pore volume significantly increased, and the corresponding values at 40 min were raised by 1677% and 1671%, respectively, compared to the raw material. At 50 min, the porosity of the sample decreased slightly as the reaction was almost finished. Besides, the average pore size of the reduced samples was slightly smaller than that of the raw material, which was attributed to the formation of micropores after reduction. The pore parameter results imply that the reduced metallic iron pores were well-developed, consistent with the SEM observations. The porous product layer was crucial in the mass transfer, which substantially reduced the internal diffusion resistance of the reaction and facilitated the successful reduction of magnetite in the boron-bearing iron concentrate at low temperatures.

Table 6. Porosity Parameter of Boron-Bearing Iron Concentrate with Different Reduction Times at 550 °C

reduction time (min)	BET surface area (m^2/g)	total pore volume (cm^3/g)	BJH average pore diameter (nm)
0	0.4754	0.0024	26.2523
5	1.3683	0.0072	22.5707
10	2.8698	0.0153	25.5768
20	6.7485	0.0292	20.2703
30	8.2007	0.0389	21.6580
40	8.4472	0.0425	22.8603
50	8.0699	0.0416	23.5142

4. CONCLUSIONS

In this study, hydrogen reduction kinetics of boron-bearing iron concentrate in a fluidized bed under low-temperature conditions were systematically discussed. The model-free method suggested that the apparent activation energy remained constant throughout the reduction with an average value of 50.67 kJ/mol. Combining the model-free and model-fitting methods, the phase boundary model R3 best described the fluidized hydrogen reduction of boron-bearing iron concentrate in the whole reduction stage, and the kinetic equation was $d\alpha/dt = 34.77\cdot\exp(-48.08/RT)\cdot(1-\alpha)^{2/3}$. Characterization of the reduction products showed that ludwigite did not participate in the reaction, which prevented the complete reduction of the boron-bearing iron concentrate at low temperatures, and the primary reaction was the reduction of magnetite to porous iron by hydrogen. The porous products were crucial in mass transfer, ensuring that hydrogen penetrated rapidly across the product layer to the

https://doi.org/10.1021/acsomega.4c02041
ACS Omega 2024, 9, 19679–19689

reaction interface. Therefore, the reaction was controlled by the reaction rate at the reaction interface. The results provided a possible and effective method for the low-temperature metallization prereduction of boron-bearing iron concentrate.

AUTHOR INFORMATION

Corresponding Author

Jianwen Yu − *School of Resources and Civil Engineering, Northeastern University, Shenyang 110819, P. R. China; State Key Laboratory of Rolling and Automation, Shenyang 110819, China; National-Local Joint Engineering Research Center of High-Efficient Exploitation Technology for Refractory Iron Ore Resources, Shenyang 110819, P. R. China;* orcid.org/0000-0002-6050-0192; Phone: +86-15942045878; Email: yujianwen@mail.neu.edu.cn

Authors

Peiyu Li − *School of Resources and Civil Engineering, Northeastern University, Shenyang 110819, P. R. China; National-Local Joint Engineering Research Center of High-Efficient Exploitation Technology for Refractory Iron Ore Resources, Shenyang 110819, P. R. China;* orcid.org/0000-0001-6980-0514

Yanjun Li − *School of Resources and Civil Engineering, Northeastern University, Shenyang 110819, P. R. China; National-Local Joint Engineering Research Center of High-Efficient Exploitation Technology for Refractory Iron Ore Resources, Shenyang 110819, P. R. China*

Peng Gao − *School of Resources and Civil Engineering, Northeastern University, Shenyang 110819, P. R. China; State Key Laboratory of Rolling and Automation, Shenyang 110819, China; National-Local Joint Engineering Research Center of High-Efficient Exploitation Technology for Refractory Iron Ore Resources, Shenyang 110819, P. R. China*

Yuexin Han − *School of Resources and Civil Engineering, Northeastern University, Shenyang 110819, P. R. China; State Key Laboratory of Rolling and Automation, Shenyang 110819, China; National-Local Joint Engineering Research Center of High-Efficient Exploitation Technology for Refractory Iron Ore Resources, Shenyang 110819, P. R. China*

Complete contact information is available at: https://pubs.acs.org/10.1021/acsomega.4c02041

Notes

The authors declare no competing financial interest.

ACKNOWLEDGMENTS

The authors are grateful for the financial support provided to this project by the National Natural Science Foundation of China (Grant nos. 52104246 and 52274253), the National Key Research and Development Program of China (Grant no. 2021YFC2902401), the Natural Science Foundation of Liaoning Province (Grant no. 2023-MS-086), and the Fundamental Research Funds for the Central Universities (Grant no. N2301013).

REFERENCES

(1) Liu, S.; Cui, C.; Zhang, X. Pyrometallurgical Separation of Boron from Iron in Ludwigite Ore. *ISIJ Int.* **1998**, *38* (10), 1077−1079.

(2) Wang, G.; Xue, Q.-g.; Wang, J.-s. Carbothermic reduction characteristics of ludwigite and boron-iron magnetic separation. *Int. J. Miner. Metall. Mater.* **2018**, *25* (9), 1000−1009.

(3) Sui, Z. T.; Zhang, P. X.; Yamauchi, C. Precipitation selectivity of boron compounds from slags. *Acta Mater.* **1999**, *47* (4), 1337−1344.

(4) Li, Z.; Han, y. Research Progress on Comprehensive Exploitation and Utilization Status of Paigeite. *Multipurpose Util. Min. Resour.* **2015**, *2*, 22−25.

(5) Han, Y.; Yu, J.; Gao, P.; Sun, Y. Reduction behavior of boron-bearing iron concentrates by bituminous coal and its magnetic separation. *Int. J. Miner. Process.* **2016**, *146*, 74−81.

(6) Guo, H.-w.; Bai, J.-l.; Zhang, J.-l.; Li, H.-g. Mechanism of Strength Improvement of Magnetite Pellet by Adding Boron-bearing Iron Concentrate. *J. Iron Steel Res. Int.* **2014**, *21* (1), 9−15.

(7) Yu, J.; Han, Y.; Gao, P.; Li, Y. Recovery of boron from high-boron iron concentrate using reduction roasting and magnetic separation. *J. Iron Steel Res. Int.* **2017**, *24* (2), 131−137.

(8) Fu, X.-j.; Chu, M.-s.; Gao, L.-h.; Liu, Z.-g. Stepwise recovery of magnesium from low-grade ludwigite ore based on innovative and clean technological route. *Trans. Nonferrous Met. Soc. China* **2018**, *28* (11), 2383−2394.

(9) Li, Y.; Gao, J.; Lan, X.; Guo, Z. Boron-Iron Separation and Boron Enrichment from Boron-Bearing Iron Concentrate at Low-Temperature Enhanced by Supergravity. *ISIJ Int.* **2022**, *62* (9), 1760−1767.

(10) Ye, L.; Peng, Z.; Tian, R.; Tang, H.; Zhang, J.; Rao, M.; Li, G. A novel process for highly efficient separation of boron and iron from ludwigite ore based on low-temperature microwave roasting. *Powder Technol.* **2022**, *410*, 117848.

(11) Wang, G.; Xue, Q. G.; Wang, J. S. Reduction of boron-bearing iron ore concentrate/coal composite pellet and kinetics analysis. *Ironmaking Steelmaking* **2016**, *43* (2), 153−162.

(12) Wang, G.; Xue, Q.-g.; Wang, J.-s. Reduction and melting separation mechanism of boron-bearing iron concentrate/coal composite pellet. *J. Iron Steel Res. Int.* **2018**, *25* (3), 310−319.

(13) Gao, P.; Li, G.; Gu, X.; Han, Y. Reduction Kinetics and Microscopic Properties Transformation of Boron-Bearing Iron Concentrate-Carbon-Mixed Pellets. *Miner. Process. Extr. Metall. Rev.* **2020**, *41* (3), 162−170.

(14) Zhang, X.; Li, G.-h.; Rao, M.-j.; Mi, H.-p.; Liang, B.-j.; You, J.-x.; Peng, Z.-w.; Jiang, T. Growth of metallic iron particles during reductive roasting of boron-bearing magnetite concentrate. *J. Cent. South Univ.* **2020**, *27* (5), 1484−1494.

(15) Li, G.; Liang, B.; Rao, M.; Zhang, Y.; Jiang, T. An innovative process for extracting boron and simultaneous recovering metallic iron from ludwigite ore. *Miner. Eng.* **2014**, *56*, 57−60.

(16) Boretti, A. The perspective of hydrogen direct reduction of iron. *J. Cleaner Prod.* **2023**, *429*, 139585.

(17) Scovell, M.; Walton, A. Identifying informed beliefs about hydrogen technologies across the energy supply chain. *Int. J. Hydrogen Energy* **2023**, *48* (82), 31825−31836.

(18) Souza Filho, I. R.; Springer, H.; Ma, Y.; Mahajan, A.; da Silva, C. C.; Kulse, M.; Raabe, D. Green steel at its crossroads: Hybrid hydrogen-based reduction of iron ores. *J. Cleaner Prod.* **2022**, *340*, 130805.

(19) Spreitzer, D.; Schenk, J. Reduction of Iron Oxides with Hydrogen—A Review. *Steel Res. Int.* **2019**, *90* (10), 1900108.

(20) Kim, S.-H.; Zhang, X.; Ma, Y.; Souza Filho, I. R.; Schweinar, K.; Angenendt, K.; Vogel, D.; Stephenson, L. T.; El-Zoka, A. A.; Mianroodi, J. R.; et al. Influence of microstructure and atomic-scale chemistry on the direct reduction of iron ore with hydrogen at 700°C. *Acta Mater.* **2021**, *212*, 116933.

(21) Hessels, C. J. M.; Homan, T. A. M.; Deen, N. G.; Tang, Y. Reduction kinetics of combusted iron powder using hydrogen. *Powder Technol.* **2022**, *407*, 117540.

(22) Kang, H.; Xu, Q.; Cao, Z.; Lu, X.; Shi, J.; Chen, B.; Guo, L. Influence of hydrogen flow rate on multistep kinetics of hematite reduction. *Int. J. Hydrogen Energy* **2024**, *49*, 1255−1268.

(23) Brandner, U.; Leuchtenmueller, M. Comparison of reduction kinetics of Fe2O3, ZnOFe2O3 and ZnO with hydrogen (H2) and carbon monoxide (CO). *Int. J. Hydrogen Energy* **2024**, *49*, 775−785.
(24) Sui, Y.-l.; Guo, Y.-f.; Jiang, T.; Qiu, G.-z. Reduction kinetics of oxidized vanadium titano-magnetite pellets using carbon monoxide and hydrogen. *J. Alloys Compd.* **2017**, *706*, 546−553.
(25) Ma, Y.; Souza Filho, I. R.; Bai, Y.; Schenk, J.; Patisson, F.; Beck, A.; van Bokhoven, J. A.; Willinger, M. G.; Li, K.; Xie, D.; et al. Hierarchical nature of hydrogen-based direct reduction of iron oxides. *Scr. Mater.* **2022**, *213*, 114571.
(26) Zhang, J.; Li, S.; Wang, L. Kinetics analysis of direct reduction of iron ore by hydrogen in fluidized bed based on response surface methodology. *Int. J. Hydrogen Energy* **2024**, *49*, 1318−1331.
(27) Schenk, J. L. Recent status of fluidized bed technologies for producing iron input materials for steelmaking. *Particuology* **2011**, *9* (1), 14−23.
(28) Pang, J.-m.; Guo, P.-m.; Zhao, P.; Cao, C.-z.; Zhao, D.-g.; Wang, D.-g. Reduction of 1−3 mm iron ore by H2 in a fluidized bed. *Int. J. Miner. Metall. Mater.* **2009**, *16* (6), 620−625.
(29) Mishra, S.; Baliarsingh, M.; Mahanta, J.; Chandra Beuria, P. Batch scale study on magnetizing roasting of low-grade iron ore tailings using fluidized bed roaster. *Mater. Today: Proc.* **2022**, *62*, 5856−5860.
(30) Du, Z.; Ge, Y.; Liu, F.; Fan, C.; Pan, F. Effect of different modification methods on fluidized bed hydrogen reduction of cohesive iron ore fines. *Powder Technol.* **2022**, *400*, 117226.
(31) Du, Z.; Liu, J.; Liu, F.; Pan, F. Relationship of particle size, reaction and sticking behavior of iron ore fines toward efficient fluidized bed reduction. *Chem. Eng. J.* **2022**, *447*, 137588.
(32) Kim, W.-H.; Lee, S.; Kim, S.-M.; Min, D.-J. The retardation kinetics of magnetite reduction using H2 and H2-H2O mixtures. *Int. J. Hydrogen Energy* **2013**, *38* (10), 4194−4200.
(33) Ding, D.; Peng, H.; Peng, W.; Yu, Y.; Wu, G.; Zhang, J. Isothermal hydrogen reduction of oxide scale on hot-rolled steel strip in 30 pct H2N2 atmosphere. *Int. J. Hydrogen Energy* **2017**, *42* (50), 29921−29928.
(34) Zuo, H.-b.; Wang, C.; Dong, J.-j.; Jiao, K.-x.; Xu, R.-s. Reduction kinetics of iron oxide pellets with H2 and CO mixtures. *Int. J. Miner. Metall. Mater.* **2015**, *22* (7), 688−696.
(35) Chen, H.; Zheng, Z.; Chen, Z.; Bi, X. T. Reduction of hematite (Fe2O3) to metallic iron (Fe) by CO in a micro fluidized bed reaction analyzer: A multistep kinetics study. *Powder Technol.* **2017**, *316*, 410−420.
(36) Zhang, Q.; Sun, Y.; Han, Y.; Li, Y.; Gao, P. Producing magnetite concentrate via self-magnetization roasting in N2 atmosphere: Phase and structure transformation, and extraction kinetics. *J. Ind. Eng. Chem.* **2021**, *104*, 571−581.
(37) Vyazovkin, S.; Burnham, A. K.; Criado, J. M.; Pérez-Maqueda, L. A.; Popescu, C.; Sbirrazzuoli, N. ICTAC Kinetics Committee recommendations for performing kinetic computations on thermal analysis data. *Thermochim. Acta* **2011**, *520* (1−2), 1−19.
(38) Wang, Z.; Zhang, J.; Jiao, K.; Liu, Z.; Barati, M. Effect of pre-oxidation on the kinetics of reduction of ironsand. *J. Alloys Compd.* **2017**, *729*, 874−883.
(39) Dilmaç, N. Isothermal and non-isothermal reduction kinetics of iron ore oxygen carrier by CO: Modelistic and model-free approaches. *Fuel* **2021**, *296*, 120707.
(40) Janković, B.; Adnađević, B.; Mentus, S. The kinetic analysis of non-isothermal nickel oxide reduction in hydrogen atmosphere using the invariant kinetic parameters method. *Thermochim. Acta* **2007**, *456* (1), 48−55.
(41) Wang, G.; Xue, Q.; She, X.; Wang, J. Carbothermal Reduction of Boron-bearing Iron Concentrate and Melting Separation of the Reduced Pellet. *ISIJ Int.* **2015**, *55* (4), 751−757.
(42) Peng, Z.-K.; Peng, Q.-M.; Ma, Y.-Q. Thermal characteristics of borates and its indication for endogenous borate deposits. *Ore Geol. Rev.* **2022**, *145*, 104887.
(43) Cao, C.-Y.; Liang, C.-H.; Yin, Y.; Du, L.-Y. Thermal activation of serpentine for adsorption of cadmium. *J. Hazard. Mater.* **2017**, *329*, 222−229.
(44) Pang, P.; Han, H.; Hu, L.; Guo, C.; Gao, Y.; Xie, Y. The calculations of pore structure parameters from gas adsorption experiments of shales: Which models are better? *J. Nat. Gas Sci. Eng.* **2021**, *94*, 104060.
(45) Wang, Z.; Zhang, J.; Zhao, B.; Fu, H.; Pang, J. Effect of pore characteristics on hydrogen reduction kinetics based on a novel analysis approach combined model-fitting and iso-conversion. *Int. J. Hydrogen Energy* **2021**, *46* (45), 23164−23173.

https://doi.org/10.1021/acsomega.4c02041
ACS Omega 2024, 9, 19679−19689